Contents lists available at ScienceDirect

Corrosion Communications

Research Article

Oxidation resistance of Mo/Cr bilayer coating on Zr alloy in a 1200 °C steam environment

Zheng Wang [a,b], Yingpeng Zhang [a,b], Shenghao Zhou [a,b], Zhenyu Wang [a,b], Yirong Yao [a,c], Aiying Wang [a,b], Ming Li [a,c,*], Peiling Ke [a,c,*]

[a] Key Laboratory of Marine Materials and Related Technologies, Zhejiang Key Laboratory of Marine Materials and Protective Technologies, Ningbo Institute of Materials Technology and Engineering, Chinese Academy of Sciences, Ningbo 315201, China
[b] Center of Materials Science and Optoelectronics Engineering, University of Chinese Academy of Sciences, Beijing 100049, China
[c] Analytical Center, Ningbo Institute of Materials Technology and Engineering, Chinese Academy of Sciences, Ningbo 315201, China

ARTICLE INFO

ABSTRACT

The Cr-coated Zr alloys demonstrate excellent resistance to high-temperature steam oxidation. However, the rapid diffusion pathways for oxygen formed by the inter-diffusion between the coating and alloy at high temperatures significantly affect the steam oxidation resistance of the coated alloys. To address this issue, we developed a Mo/Cr bilayer coating on Zr alloy by a combination of dc-MS and HiPIMS surface treatments. The coating exhibits outstanding steam oxidation resistance at high temperatures, resulting in a mass gain approximately 86.6% and 44.1% lower than that of the bare Zr alloy and Cr coating, respectively, after 30 min of steam oxidation at 1200 °C. This is mainly because, during the oxidation process, the Mo interface layer undergoes a transformation into a thin and high-quality double diffusion layer structure, effectively avoiding high-temperature inter-diffusion between the Cr coating and Zr alloy, thereby inhibiting the formation of oxygen diffusion pathways.

1. Introduction

Zr alloy is a popular choice for nuclear fuel cladding materials due to its low thermal neutron absorption cross-section [1], good thermal conductivity [2] and mechanical properties [3], and excellent resistance to corrosion in high-temperature aqueous solutions [4]. However, during a loss-of-coolant accident (LOCA) [5] in a pressurized water reactor (PWR) power station, the flow of coolant in the core is interrupted, causing the temperature of the fuel element to rise rapidly. In this high-temperature environment, the Zr alloy cladding reacts with steam, leading to severe oxidation and the generation of a significant amount of hydrogen. The accumulation of hydrogen can cause a "hydrogen explosion" and ultimately result in nuclear leakage [6,7]. Surface protective coatings are viewed as a highly promising strategy for enhancing the safety of accident-tolerant fuels (ATFs). This approach is both reliable and cost-effective, as it can effectively suppress the reaction between steam and Zr alloy cladding, thereby delaying or potentially preventing LOCA disasters. The findings from previous research indicate that the high-temperature steam oxidation resistance of Zr alloy

can be significantly enhanced by utilizing a Cr coating [8–10], which is more effective than FeCrAl [11,12], MAX phase [13–15], and SiC [16] coatings.

In recent years, there have been multiple different methods for preparing Cr coatings on Zr alloys, including chemical vapor deposition (CVD), physical vapor deposition (PVD), laser beam, spraying, and others [17–20]. Among these methods, the Cr coating produced by PVD technology, which includes arc ion plating (AIP), direct current magnetron sputtering (dc-MS), and high-impulse-power magnetron sputtering (HiPIMS), is distinguished by its thin and dense structure, making it highly compatible with the requirements for neutron economy and oxidation resistance of the cladding. Moreover, studies [21,22] have demonstrated that the Cr coating deposited by HiPIMS technology possesses a dense structure with very fine grains, while the Cr coating deposited by traditional dc-MS exhibits a porous structure with coarse grains. Additionally, the Cr coating deposited by HiPIMS technology displays no significant large particles on the surface and exhibits superior oxidation resistance in high-temperature steam environments in comparison to AIP [23]. Therefore, the application of HiPIMS technology

---

* Corresponding authors.
E-mail addresses: liming@nimte.ac.cn (M. Li), kepl@nimte.ac.cn (P. Ke).

for Cr coating deposition on Zr alloys represents a promising approach to enhance the performance of nuclear fuel cladding materials.

However, the Cr-coated Zr alloy cladding may experience severe element interdiffusion during a loss-of-coolant accident (LOCA). Specifically, Cr can diffuse into the Zr substrate, resulting in the formation of a brittle Zr-Cr interdiffusion layer [9,24,25] and a reduction in the toughness of the coating-substrate system. Meanwhile, the diffusion of Zr along the grain boundary of the Cr coating can create rapid diffusion paths of oxygen [26], leading to damage and failure of the Cr coating. To avoid these problems, it is necessary to construct a diffusion barrier between the Cr coating and Zr substrate.

There have been several studies performed on the interface design between Zr alloy and protective coatings. Tang et al. [27] prepared a 500 nm TiC interface layer between a Zry-4 alloy and a 5.5 μm Ti_2AlC coating. They noted that the TiC layer offered some degree of resistance to the diffusion of Al, but the impact was relatively limited. Al was still able to diffuse through the TiC grain boundary and reach the Zry-4 alloy substrate, leading to the complete consumption of the Ti_2AlC/TiC bilayer coating after steam oxidation at 1000 °C for 5 min. Additionally, Wang et al. [28] developed an MAO/Cr composite coating on Zr-1Nb alloy. Their research showed that the MAO interface layer effectively prevented interdiffusion between the substrate and top Cr coating, thereby improving the accident tolerance of Cr-coated Zr-1Nb alloy cladding. However, at high temperatures, the oxygen element in the MAO interface layer diffused to the substrate, causing the near-surface β-Zr phase to transform to the brittle α-Zr(O) phase and leading to volume expansion, which ultimately promoted the initiation and propagation of substrate cracks. The diffusion rate of Mo is relatively low and the thermal expansion coefficients of Mo and Zr are similar, making it one of the highly sought-after interface layer materials. Han et al. [11] introduced a Mo interface layer between Zry-4 alloy and FeCrAl coating, and found that the Mo/FeCrAl bilayer coating protected the substrate from oxidation after 60 min of high-temperature steam corrosion at 1200 °C. However, Fe and Cr diffused rapidly into the Mo interface layer during oxidation, resulting in the formation of an intermetallic FeCrMo layer at the Mo/FeCrAl interface and numerous Kirkendall voids inside the residual FeCrAl layer. Syrtanov et al. [29] deposited a 3 μm Mo interlayer between a Zr alloy and an 8 μm Cr coating using dc-MS. High-temperature steam oxidation tests at 1200–1400 °C demonstrated that

the Mo/Cr bilayer coating exhibited superior oxidation resistance compared to a single Cr coating. Since the Cr coating deposited by HiPIMS technology is denser than that deposited by dc-MS technology, it is expected that the Mo/Cr bilayer coating, with the Mo interlayer deposited by dc-MS and the top Cr layer deposited by HiPIMS, will exhibit better oxidation resistance. In addition, the oxidation kinetics and microstructure evolution mechanism of Mo/Cr-coated Zr alloy in high-temperature steam environments remain uncovered yet.

Hence, in this work, a Mo/Cr bilayer coating on Zr alloy was fabricated by a combination of dc-MS and HiPIMS surface treatments. The steam oxidation properties of bare, Cr-coated and Mo/Cr-coated Zr alloys at 1200 °C were compared. Furthermore, the influence mechanism of Mo interlayer on the steam oxidation behavior of Mo/Cr-coated Zr alloy was analyzed.

2. Experimental

2.1. Sample preparation

Commercial zirconium alloy (wt.%; 1.0% Sn, 1.0% Nb, 0.1% Fe, balance Zr) with dimensions of 15 mm × 10 mm × 2 mm was used as the substrate. Prior to coating deposition, the substrate was polished to #3000 using SiC sandpaper. Then, the samples were ultrasonically cleaned in acetone and anhydrous ethanol for 15 min, respectively.

The Mo/Cr composite coating was deposited by a self-developed magnetron sputtering system (Fig. 1). When the base pressure of the vacuum chamber was below 3.7×10^{-3} Pa, Ar^+ etching was then performed (for 15 min) to remove surface contaminants. The Mo/Cr composite coating was fabricated in a magnetron sputtering chamber including two cathodes. A Mo target (380 mm × 100 mm × 7 mm, 99.999 wt.%) was mounted on a cathode driven by a 1.0 kW DC power supply for 200 min. In addition, a chromium target (380 mm × 100 mm × 7 mm, 99.999 wt.%) was mounted on another cathode driven by a HiPIMS power supply with a power of 3.0 kW for 420 min. During the deposition process, the chamber temperature was maintained at 200 °C and a bias voltage of −80 V was applied to the substrate. In addition, the single Cr coating was also prepared on the Zr alloy substrate as a control group.
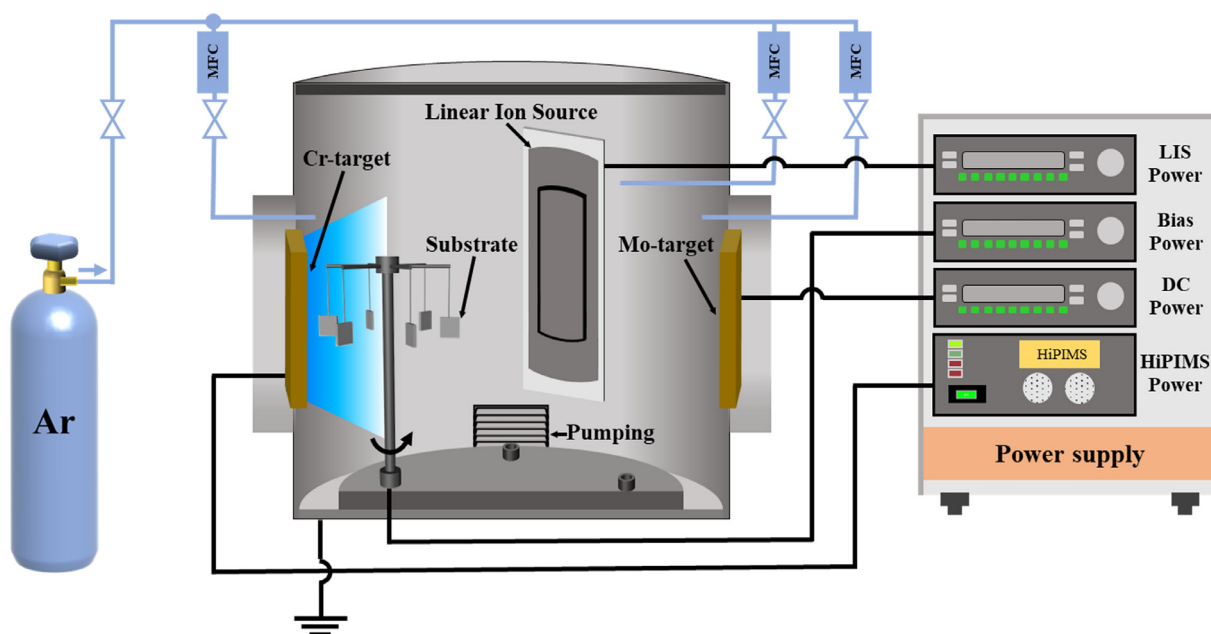

Fig. 1. Schematic of the Mo/Cr coating deposition system.

2.2. Steam oxidation of Cr-coated and Mo/Cr-coated Zr alloys

Steam oxidation tests were conducted on Zr alloy substrate, Cr and Mo/Cr coatings by a thermogravimetric analyzer (TGA, SETARAM SET-SYS). Specifically, steam with Ar carrier gas was introduced into the furnace at a total rate of 50 mL/min and relative humidity of 4%. Meanwhile, the temperature was increased from 900 °C to 1200 °C at a heating rate of 15 °C/min and held for 30 min.

2.3. Characterization method

The crystal structures of the specimens were characterized by X-ray diffraction (XRD, D8 Advance diffractometer), employing Cu K_α radiation and a 0.02° step in the conventional $\theta-2\theta$ configuration. The microstructures and compositions were examined by a scanning electron microscope (SEM, Verios G4 UC) equipped with energy dispersive spectrometer (EDS) and electron back-scattered diffraction (EBSD) detectors. The cross-sectional SEM and EBSD samples were grinded with SiC sandpaper up to 3000#, followed by mechanical polishing and Ar+ milling, respectively. In addition, the cross-section samples after steam oxidation were etched in a mixed acid solution containing 1.0% HF, 1.5% HCl, 2.5% HNO$_3$, and 95% H$_2$O (in vol.%), and then observed by SEM. To further clarify the phase composition of the samples after steam oxidation, a Talos F200 transmission electron microscope (TEM) was performed at the acceleration voltage of 200 kV. The cross-sectional TEM specimens were prepared by using a focused ion beam system (FIB, Auriga).

3. Results and discussion

3.1. Steam oxidation resistance

Fig. 2 shows the oxidation kinetics curves of Zr substrate, Cr and Mo/Cr coatings in a steam environment at 1200 °C. As shown in Fig. 2(a), the whole oxidation process can be separated into heating process (Stage I) and holding process (Stage II) at 1200 °C. A rapidly increasing oxidation mass gain was observed for bare Zr alloy in the whole scope. In comparison, the oxidation mass gains of Cr and Mo/Cr coatings did not show significant changes during Stage I, and they both increased slowly during Stage II. Notably, the Mo/Cr coating showed a significantly slower increase compared to the Cr coating. Ultimately, after 30 min of steam oxidation at 1200 °C, the Mo/Cr bilayer coating displayed a mass gain of approximately 86.6% and 44.1% lower than that of the bare Zr alloy and Cr coating, respectively. To further evaluate the steam oxidation resistance of samples during holding process at 1200 °C, the change of mass gain rate with oxidation time was also obtained, as shown in Fig. 2(b). It should be noted that the bare and

Mo/Cr coating maintained a relatively stable mass gain rate, whereas the Cr coating exhibited an increased mass gain rate over time. This can be attributed to the formation of multiple fast-diffusion paths for oxygen inside the residual Cr coating during oxidation of the Cr coating [26]. In addition, the study found that the Mo/Cr coating had a lower average mass gain rate (5.87×10^{-5} g/(cm^2·min)) compared to the bare Zr alloy (3.82×10^{-4} g/(cm^2·min)). Therefore, it can be seen that the Mo/Cr bilayer structure has significant advantages over the pure Cr monolayer structure and bare Zr alloy in terms of steam oxidation resistance at 1200 °C.

3.2. Structure and composition of coating

Fig. 3 shows the XRD patterns and texture coefficients of the Cr and Mo/Cr coatings. The diffraction peaks in Fig. 3(a) were consistent with body-center cubic (BCC) Cr. Moreover, the preferred orientation of the two coatings showed similar crystal characteristics. To quantitatively identify the preferred orientation of Cr and Mo/Cr coatings, the texture coefficient (TC) was defined by the following formula [30]:

$$TC = \frac{I_{(hkl)}/I_{0(hkl)}}{\sum \left[I_{(hkl)}/I_{0(hkl)} \right]} \tag{1}$$

where I_0 and I are the diffraction peaks in a standard PDF card at a crystal plane and the actual intensity of the diffraction peaks at the crystal plane, respectively. Fig. 3(b) illustrates the calculation results of specific texture coefficients for Cr and Mo/Cr coatings. In general, the larger number of texture coefficients replies to the strongly preferred phase orientation in crystals [10]. It was interesting that both Cr and Mo/Cr coatings were dominated by the (110)-preferred orientation, even the higher texture coefficient of (110) crystal plane was observed for Mo/Cr coating at 0.955 than that of Cr coating at 0.815 for comparison. For the Cr grains with BCC lattices, the lowest surface energy and strain energy were assigned to (110) crystal plane and (200) crystal plane, respectively [31]. It should be noted that HiPIMS technique with a relatively low plasma energy and a slow deposition rate can promote the lateral growth of low-surface-energy oriented grains, and subsequently lead to the formation of a strong (110) texture. However, the lattice mismatch strain would stimulate the crystal growth of Cr coating along the minimum strain-energy crystal plane. Compared to the HCP-Zr/BCC-Cr heterointerface, the BCC-Mo/BCC-Cr heterointerface showed a relatively smaller lattice mismatch ratio (η). Thus, the Cr coating showed a stronger (200) texture than that of the Mo/Cr coating.

Fig. 4 shows the surface and cross-sectional morphologies of the Cr and Mo/Cr coatings. As shown in Fig. 4(a) and (d), both the Cr and Mo/Cr coatings exhibited smooth surfaces without any macro-particles, which can be attributed to the high plasma density of the HiPIMS dis-
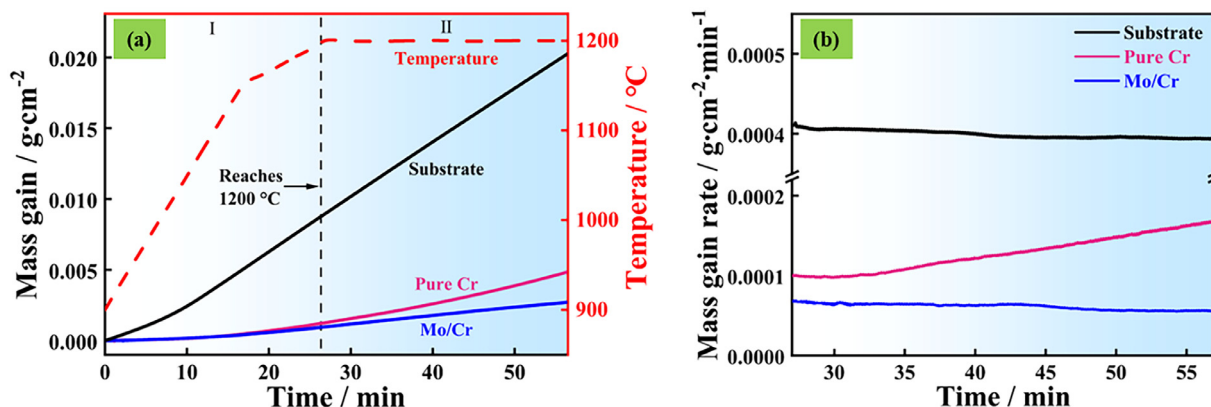

Fig. 2. (a) Mass gain and (b) mass gain rate over oxidation time of bare, Cr and Mo/Cr coatings in 1200 °C steam environment.
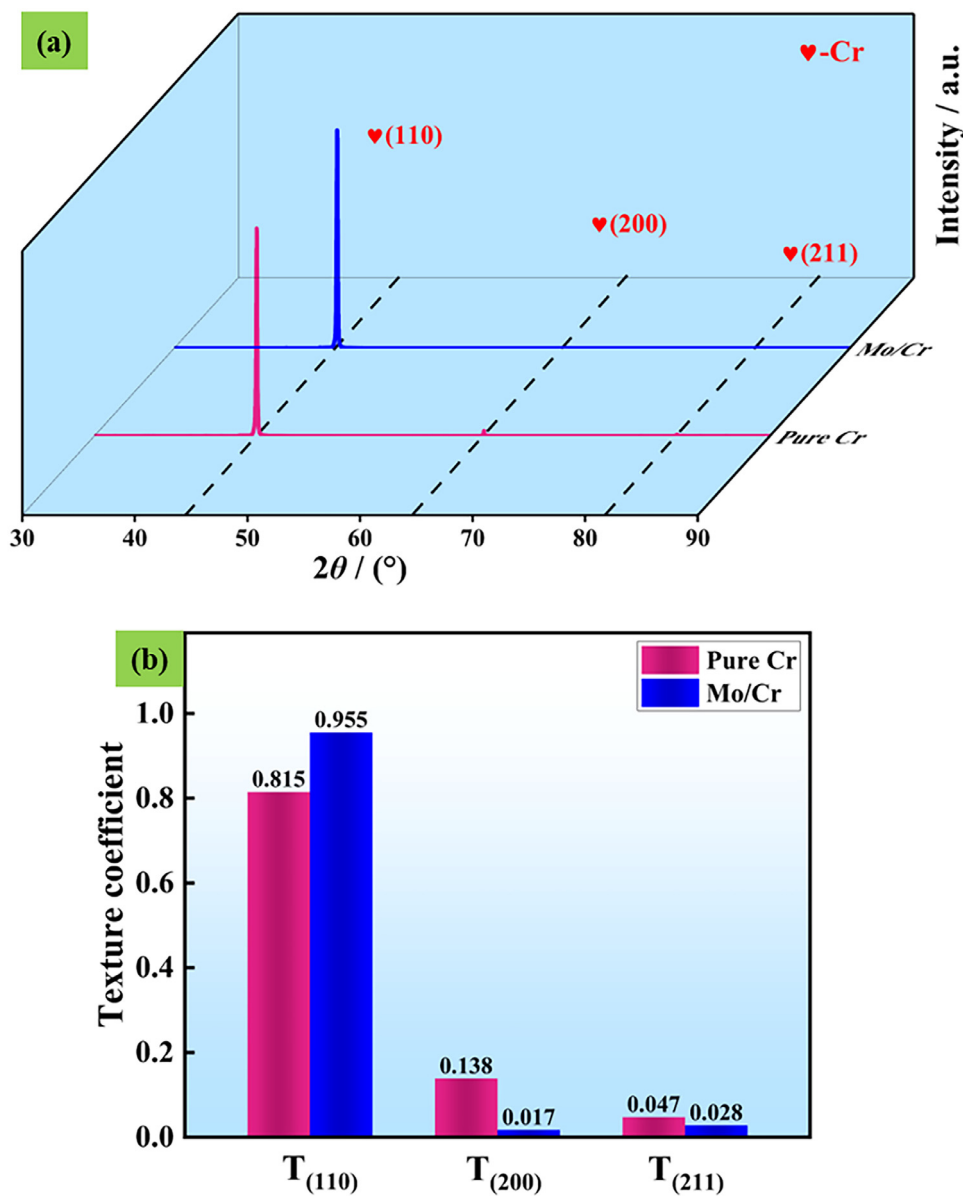
Fig. 3. (a) XRD patterns and (b) texture coefficients of Cr and Mo/Cr coatings.

charge with a Cr target [32,33]. The corresponding cross-sectional morphologies are shown in Fig. 4(b) and (e). It can be seen that both the coatings were uniform and well-adhered to the Zr substrates. The thickness of a single Cr coating (Fig. 4(b)) was 9.78 μm. Fig. 4(e) displays the cross-section of as-grown Mo/Cr coating. It can be observed that the thickness of the top Cr layer and Mo interlayer was ~9.82 and ~3.17 μm, respectively.

Since SEM measurements were not sufficient to obtain the detailed crystallography details, EBSD tests were performed to gain insight into the variation of grain size and crystallographic shape of the different coatings. As shown in Fig. 5, Cr and Mo/Cr coatings were very similar and both exhibited refined dense columnar crystals. Interestingly, the mean grain size of the Mo interlayer was much smaller than that of the top Cr layer, which was attributed to the decreased atomic diffusion mobility at the process of dc-MS discharge with a Mo target.

3.3. Analysis of the oxidation morphologies and phase compositions

The surface and cross-sectional oxidation morphologies of Cr and Mo/Cr coatings after oxidation at 1200 °C for 30 min are shown in Fig. 6.

After oxidation, many particles appeared on the surfaces of the Cr and Mo/Cr coatings (Fig. 6(a, d)), which can be attributed to the spalling of oxides during the cooling process. Moreover, the quantity of spalling oxides on the Mo/Cr coating was significantly lower than that of the Cr coating. The cross-sectional morphologies and EDS results of the oxidized Cr coating and Mo/Cr coating are shown in Fig. 6(b, c, e, f). It should be noted that numerous micro-pores were observed within the scales of both the Cr and Mo/Cr coatings, which can be attributed to the evaporation of gaseous CrO_3 and $CrO_2(OH)_2$ [34]. Despite experiencing different levels of oxidation damage during the harsh steam test, the Cr element on both the Cr and Mo/Cr coatings had residual thicknesses of approximately 3.57 and 6.57 μm, respectively. In fact, the close-packed (110) orientation exhibited the highest reticular density compared to the (200) and (211) textures for BCC-Cr. Additionally, the Mo/Cr coating demonstrated a higher texture coefficient for the (110) crystal plane in comparison to the Cr coatings. Therefore, the Mo/Cr coating with an intense (110) texture can more effectively impede the penetration of external oxygen and provide superior protection to the substrate. In addition, a one-layer Zr-Cr interdiffusion layer was assigned to the Cr coating, while the Mo/Cr coating was assigned a bi-
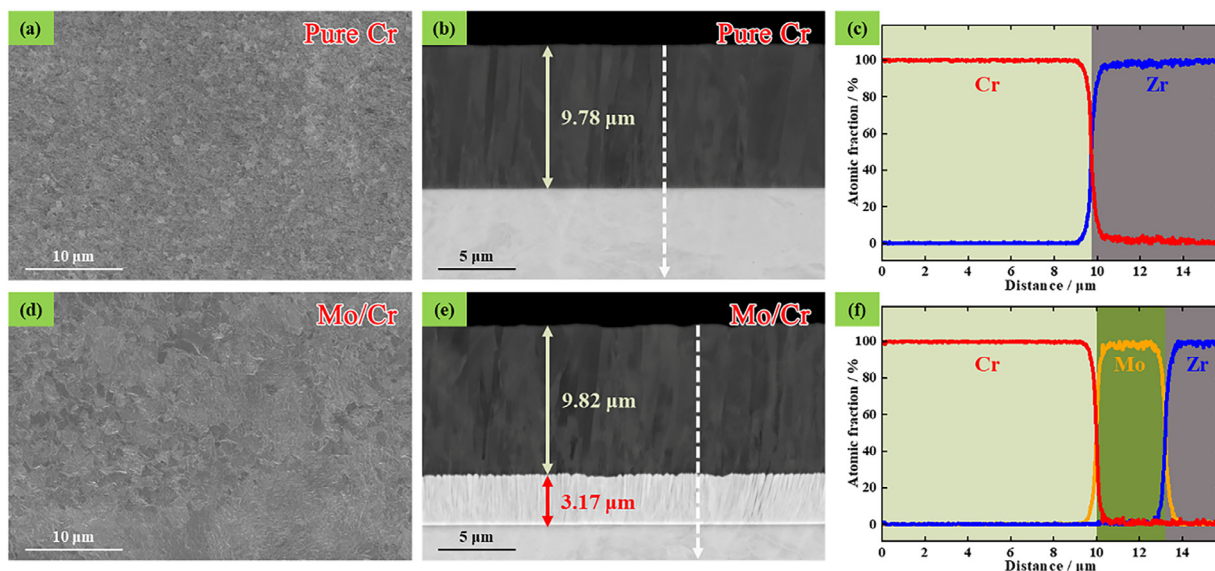
Fig. 4. (a, d) Surface and (b, e) cross-sectional SEM images of (a, b) the Cr and (d, e) Mo/Cr coatings and (c, f) the corresponding EDS scan along the white line in Fig. 4(b) and (e), respectively.
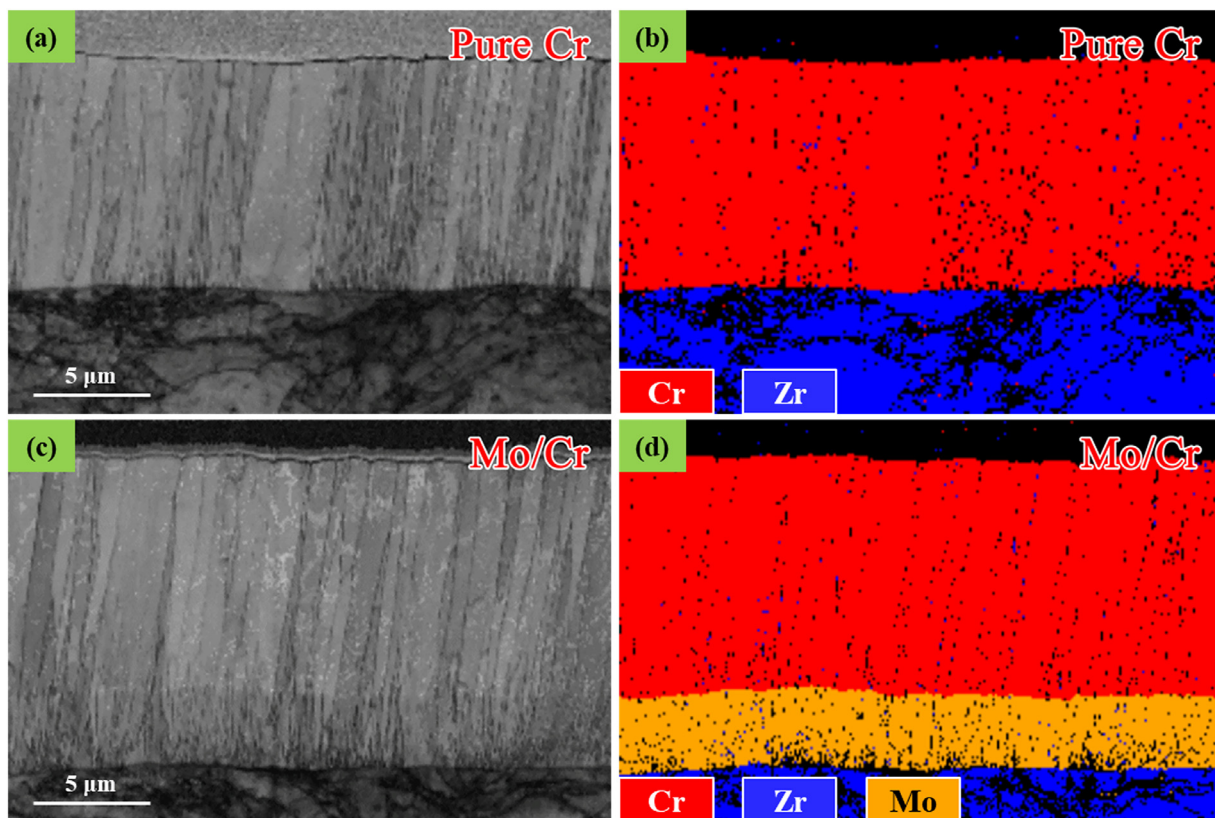

Fig. 5. (a, c) Band contrast maps and (b, d) corresponding EBSD phase maps for the (a, b) Cr-coated Zr alloy and (c, d) Mo/Cr-coated Zr alloy.

level Cr-Mo-Zr interdiffusion layer. This can be attributed to the diffusion of elements at the interface between the prepared coatings and Zr substrate.

Previous research has shown that steam reacts with Zr alloy at high temperatures, leading to the formation of a surface layer of ZrO_2 oxide scale and an intermediate layer of oxygen-stabilized α-Zr(O) [35]. To further evaluate the oxygen permeation resistance of bare, Cr and Mo/Cr coatings, corresponding cross-sectional SEM analysis was performed after high-temperature steam oxidation and chemical corrosion,

as shown in Fig. 7. Compared to the bare Zr alloy (109.56 μm), the Cr coating exhibited a significantly thinner α-Zr(O) layer, while the Mo/Cr coating did not exhibit an obvious α-Zr(O) layer. Considering that the initial thickness of the top Cr layer was 9.78 and 9.82 μm of the Cr coating and Mo/Cr coating prior to the steam test, it can be concluded that the Mo/Cr coating had better oxidation resistance than the Cr coating.

To obtain additional crystallographic details of the Cr and Mo/Cr coatings after 30 min of steam oxidation at 1200 °C, a combined EBSD
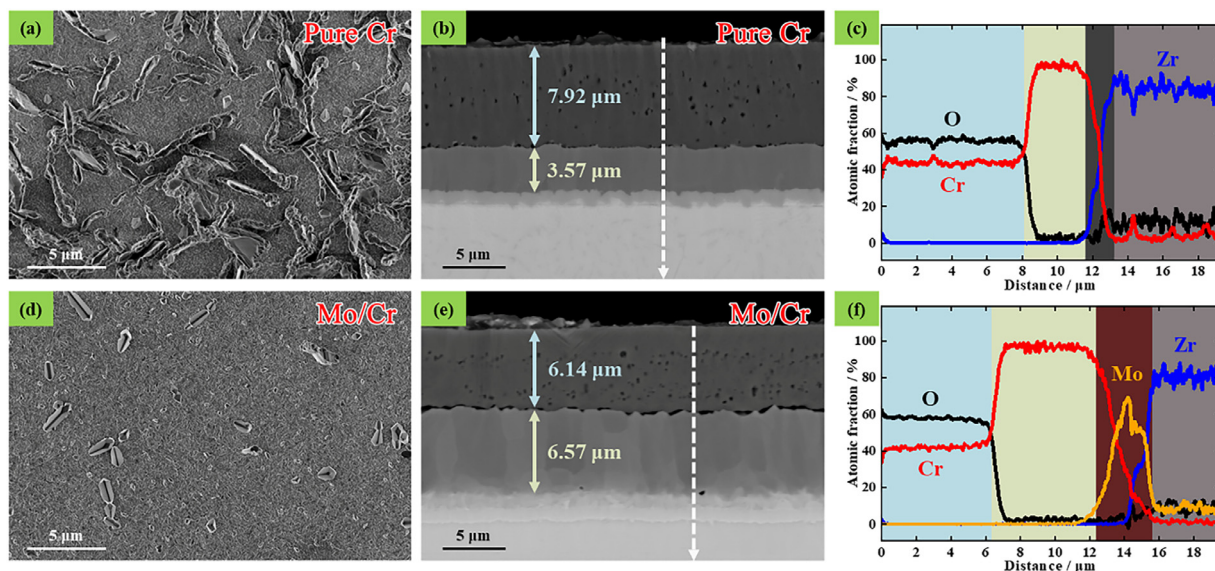
Fig. 6. (a, d) Surface, (b, e) cross-sectional SEM images and (c, f) corresponding EDS scan along the white line in Fig. 6(b) and (e) of the Cr coating (a-c) and Mo/Cr coating (d-f) oxidized at 1200 °C for 30 min.
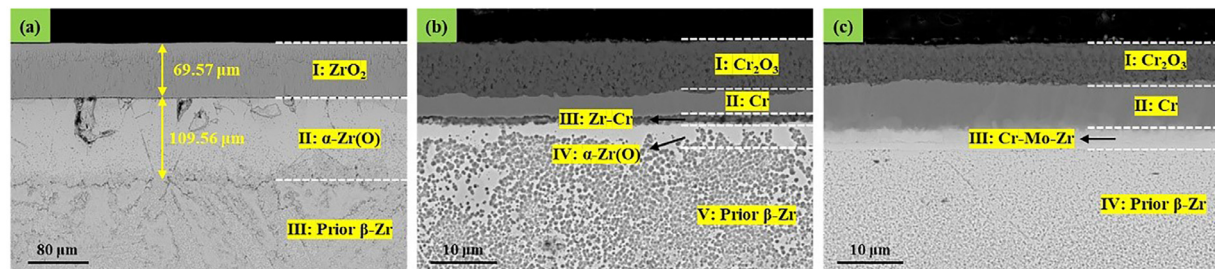

Fig. 7. Cross-section SEM images of (a) bare, (b) Cr and (c) Mo/Cr coatings oxidized at 1200 °C for 90 min, followed by chemical corrosion.

and EDS analytical technique was utilized. As shown in Fig. 8(a) and (c), a columnar to equiaxed transition (CET) occurred in the residual Cr of both the Cr and Mo/Cr coatings, which was caused by the re-crystallization and growth of grains during oxidation [26,36]. In addition, a distinct Cr_2O_3 oxide scale with an obvious equiaxed crystal structure formed on the surfaces of both the Cr and Mo/Cr coatings. It should be noted that the Mo/Cr coating exhibited significantly finer equiaxed Cr_2O_3 grains compared to the Cr coating. In fact, the formation of Cr_2O_3 grains requires the diffusion of oxygen into the coating and the re-precipitation of Cr_2O_3 particles onto existing grains. By blocking the diffusion of oxygen, the close-packed Cr (110) orientation can prevent the growth of Cr_2O_3 grains, thereby improving the stability and durability of the coating. Moreover, the fine-grained oxides were prone to release thermal stress during cooling via diffusion creep [37]. This may be the primary reason why the surface oxides of Mo/Cr coating exhibited superior adhesion compared to Cr coating (Fig. 6(a), (d)). Fig. 8(b) shows the corresponding EBSD phase map of the Cr-coated Zr alloy oxidized at 1200 °C for 30 min. The results indicated that the Zr-Cr transition layer primarily consisted of a face-centered cubic (FCC) $ZrCr_2$ phase. Fig. 8(c) shows the band contrast map and EDS mappings of the Cr coating oxidized at 1200 °C for 30 min. The double-layer interdiffusion coating of Cr-Mo-Zr comprised a columnar interdiffusion layer of Cr-Mo and a nanocrystalline interdiffusion layer of Mo-Zr, which together hindered the diffusion of external oxygen to the underlying Zr alloy.

The TEM results of the residual Cr for the Cr coating and Mo/Cr coating after 30 min of steam oxidation at 1200 °C are shown in Fig. 9. After high-temperature steam oxidation, distinct ZrO_2 grains were precipitated at the grain boundaries of the residual Cr in the Cr coating

(Fig. 9(a)). These grains were interconnected to form a network that facilitated fast diffusion paths for oxygen [26]. According to the TEM bright-field image and SAED image in Area 1 (Fig. 9(c-f)), it was observed that the residual Cr and ZrO_2 precipitates have body-centered cubic and monoclinic structures, respectively. Moreover, the orientation relationship between the BCC-Cr phase and M-ZrO_2 phase was determined to be [100]Cr//[110]ZrO_2. In fact, the formation of M-ZrO_2 phase within the residual Cr can be attributed to the diffusion of Zr along the grain boundary of the Cr coating and its preferential reaction with oxygen during the oxidation process. In contrast, no ZrO_2 precipitates were detected within the grains or at the grain boundaries of the residual Cr in the Mo/Cr coatings after oxidation (Fig. 9(b)). The important reason was that the formed double-layer interdiffusion coating of Cr-Mo-Zr effectively eliminated the high-temperature inter-diffusion between Cr coating and Zr alloy. These results further confirm that the Mo/Cr coating exhibited superior resistance to steam oxidation compared to the Cr coating at 1200 °C.

To further determine the phase composition of the newly-formed double Cr-Mo-Zr diffusion layer during oxidation, TEM characterization was performed on the corresponding regions. As shown in Fig. 10(a), the Cr-Mo-Zr diffusion layer consisted of two parts: a columnar Cr-Mo interdiffusion layer and a nanocrystalline Mo-Zr interdiffusion layer. By analyzing the corresponding HRTEM bright-field and SAED images (Fig. 10(b-e)), it can be concluded that the interdiffusion layers of Cr-Mo and Mo-Zr were composed of a base-centered orthorhombic (BCO) CrMo phase and a face-centered cubic (FCC) Mo_2Zr phase, respectively. It should be noted that the presence of the CrMo and Mo_2Zr double-layer structure in the Cr-Mo-Zr diffusion layer effec-
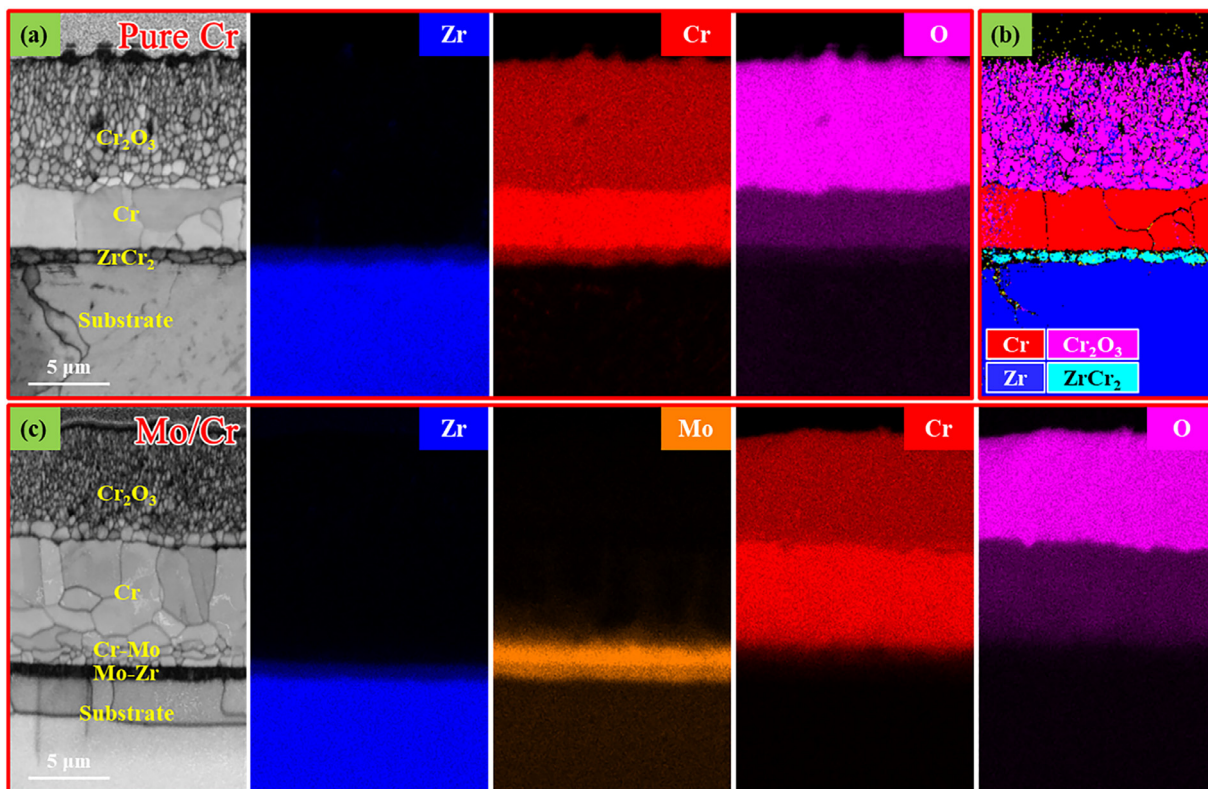
Fig. 8. (a, c) Cross-sectional EBSD patterns and (b) corresponding EDS mappings of (a, b) Cr and (c) Mo/Cr coatings oxidized at 1200 °C for 30 min.
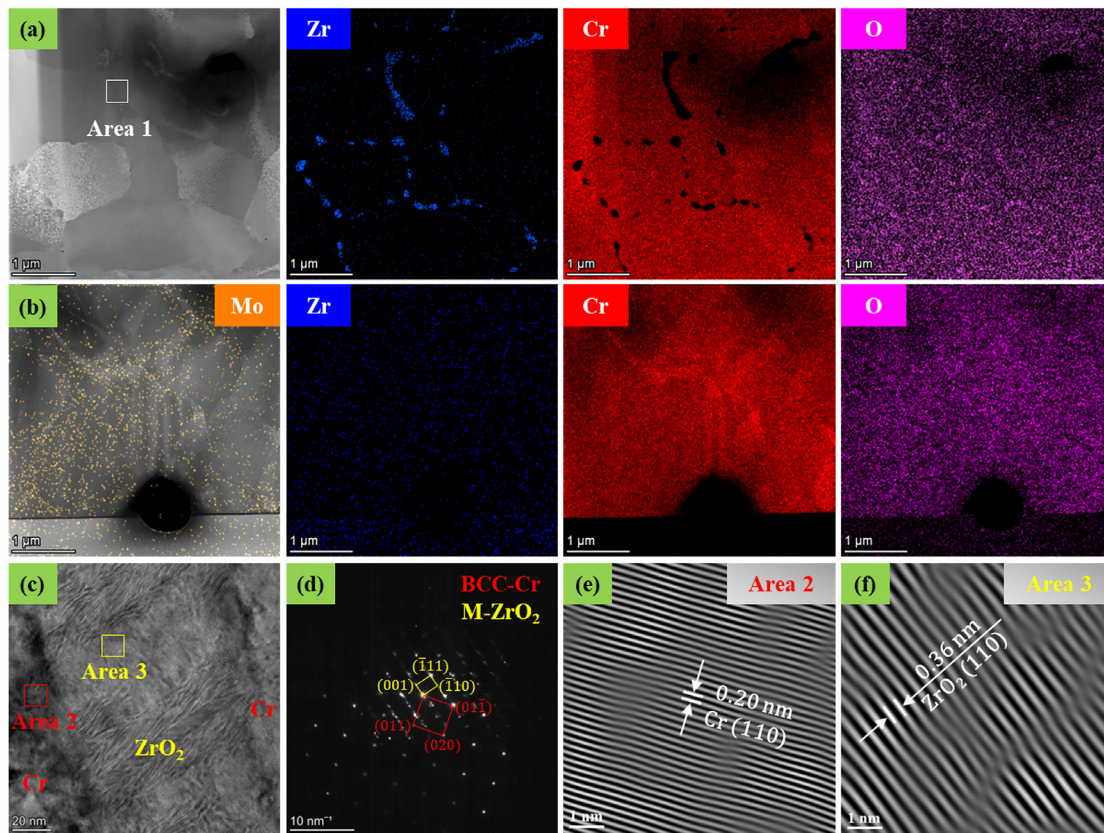

Fig. 9. TEM results of the residual Cr in both the Cr and Mo/Cr coatings oxidized at 1200 °C for 30 min: (a, b) STEM images with corresponding EDS mappings of Cr and Mo/Cr coatings, (c, d) TEM bright-field image and SAED image of Area 1 in Fig. 9(a), (e, f) enlarged images of the labeled area in Fig. 9(c).
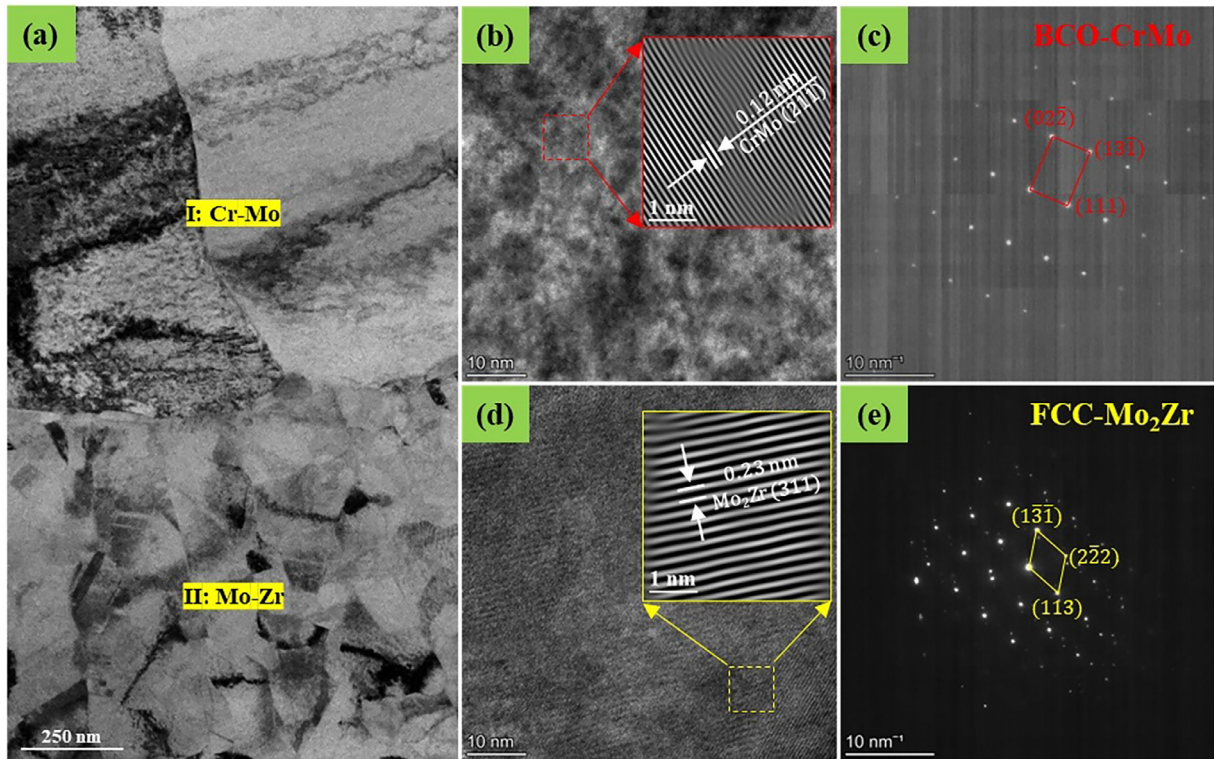
Fig. 10. TEM results of the double Cr-Mo-Zr diffusion layer in the Mo/Cr coating oxidized at 1200 °C for 30 min: (a) TEM bright-field image of the double Cr-Mo-Zr diffusion layer, (b, c) HRTEM bright-field image and SAED image of the Cr-Mo interdiffusion layer respectively, (d, e) HRTEM bright-field image and SAED image of the Mo-Zr interdiffusion layer.
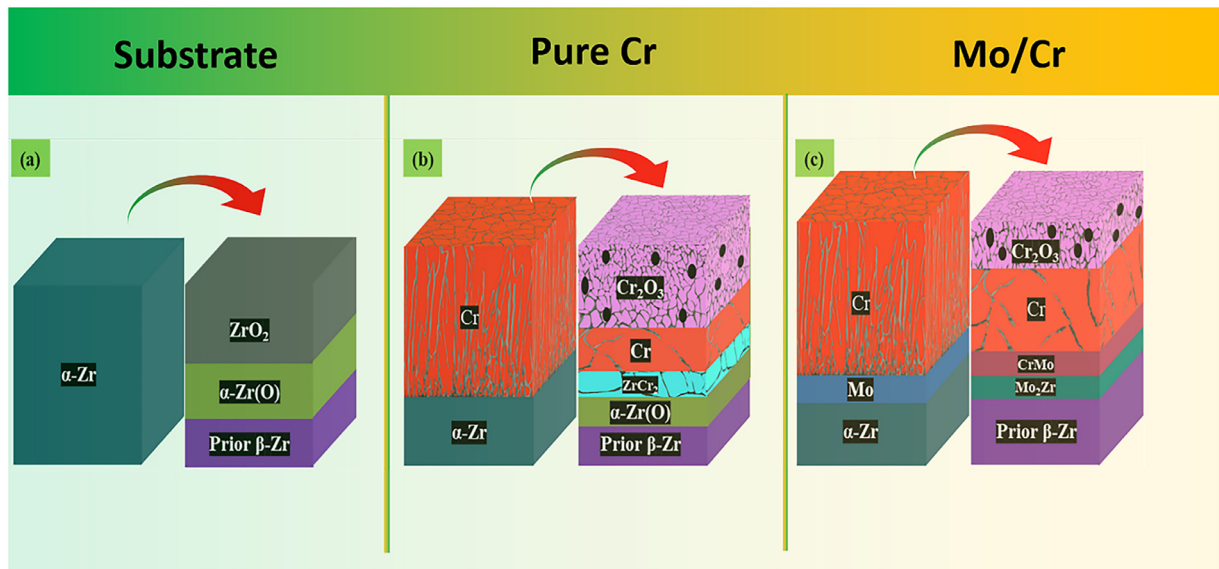

Fig. 11. Schematic diagrams of the (a) bare, (b) Cr coating, and (c) Mo/Cr coating before and after oxidized at 1200 °C for 30 min.

tively hindered the diffusion of Zr to the Cr layer. This was because the double-layer structure acted as a diffusion barrier that prevented the movement of atoms between the layers. The CrMo and Mo_2Zr layers had different crystal structures and lattice parameters, which made it difficult for atoms to cross the interface. Furthermore, the presence of the double-layer structure promoted the formation of a stable Cr_2O_3 oxide scale on the surface, further enhancing the barrier properties of the coating. In short, the CrMo and Mo_2Zr double-layer structure was an effective way to improve the diffusion resistance of

coatings and prevent the degradation of materials in high-temperature environments.

The schematic diagrams of bare, Cr, and Mo/Cr coatings before and after oxidizing at 1200 °C for 30 min are illustrated in Fig. 11. After high-temperature steam oxidation, it was observed that all samples exhibited distinctly different layered structures. Compared to the ZrO_2 scale, the Cr_2O_3 scale formed on the Cr coating or Mo/Cr coating surface was more efficient in inhibiting the diffusion of external oxygen to the underlying Zr alloy. This difference can be attributed to the higher stability

and lower growth rate of Cr_2O_3 in comparison to ZrO_2. Hence, both the Cr and Mo/Cr coatings demonstrated excellent resistance to steam oxidation at 1200 ˚C. Furthermore, the Mo/Cr coating exhibited a thinner and finer-grained Cr_2O_3 scale, which was closely related to the relatively higher (110) texture intensity before oxidation and the formation of a diffusion barrier with a CrMo and Mo_2Zr double-layer structure during oxidation.

4. Conclusions

In summary, we successfully fabricated Mo/Cr bilayer coating on Zr alloy via a combination of dc-MS and HiPIMS surface treatments. The steam oxidation resistance of the bare, Cr and Mo/Cr coatings at 1200 ˚C was comparatively studied. The key conclusions of this research can be summarized as follows:

1. The Mo/Cr coating showed a stronger (110) texture than that of Cr coating. In addition, a columnar to equiaxed transition (CET) occurred in the residual Cr of both the Cr-coated and Mo/Cr coatings.
2. After 30 min of steam oxidation at 1200 ˚C, the Mo/Cr bilayer coating exhibited a mass gain of approximately 86.6% and 44.1% lower than that of the bare Zr alloy and Cr coating, respectively.
3. The Mo interlayer enhanced the steam oxidation resistance of the Cr coating by improving the adhesion and compactness of the Cr_2O_3 scale, as well as by promoting the formation of a CrMo and Mo_2Zr double-layer structure.

Declaration of competing interest

The authors declare that they have no known competing financial interests or personal relationships that could have appeared to influence the work reported in this paper.

Acknowledgments

References

[1] K.A. Terrani, Accident tolerant fuel cladding development: promise, status, and challenges, J. Nucl. Mater. 501 (2018) 13–30.

[2] V.E. Peletsky, High-temperature thermal conductivity of zirconium-based alloys, High Temp.-High Press. 31 (1999) 627–632.

[3] X.Y. Chen, D. Wang, B.D. Yao, L. Wu, X.Y. Wu, Y.X. Wang, Mechanical and thermal properties of zirconium claddings after doping niobium: understanding from first-principles calculations, J. Nucl. Mater. 568 (2022) 153876.

[4] J.Y. Park, B.K. Choi, Y.H. Jeong, Y.H. Jung, Corrosion behavior of Zr alloys with a high Nb content, J. Nucl. Mater. 340 (2005) 237–246.

[5] X. Wu, W. Li, Y. Zhang, W. Tian, G. Su, S. Qiu, Analysis of the loss of pool cooling accident in a PWR spent fuel pool with MAAP5, Ann. Nucl. Energy 72 (2014) 198–213.

[6] N. Fujisawa, S. Liu, T. Yamagata, Numerical study on ignition and failure mechanisms of hydrogen explosion accident in Fukushima Daiichi Unit 1, Eng. Fail. Anal. 124 (2021) 105388.

[7] J. Yanez, M. Kuznetsav, A. Souto-Iglesias, An analysis of the hydrogen explosion in the Fukushima-Daiichi accident, Int. J. Hydrog. Energy 40 (2015) 8261–8280.

[8] J.-H. Park, H.-G. Kim, J.-Y. Park, Y.-I. Jung, D.-J. Park, Y.-H. Koo, High temperature steam-oxidation behavior of arc ion plated Cr coatings for accident tolerant fuel claddings, Surf. Coat. Technol. 280 (2015) 256–259.

[9] X. Han, C. Chen, Y. Tan, W. Feng, S. Peng, H. Zhang, A systematic study of the oxidation behavior of Cr coatings on Zry4 substrates in high temperature steam environment, Corros. Sci. 174 (2020) 108826.

[10] Y. Meng, S. Zeng, Z. Teng, X. Han, H. Zhang, Control of the preferential orientation Cr coatings deposited on zircaloy substrates and study of their oxidation behavior, Thin Solid Films 730 (2021) 138699.

[11] X. Han, Y. Wang, S. Peng, H. Zhang, Oxidation behavior of FeCrAl coated Zry-4 under high temperature steam environment, Corros. Sci. 149 (2019) 45–53.

[12] J.-M. Kim, T.-H. Ha, J.-S. Park, H.-G. Kim, Effect of laser surface treatment on the corrosion behavior of FeCrAl-coated TZM alloy, Metals 6 (2016) 29.

[13] J. Zhang, Z. Tian, H. Zhang, L. Zhang, J. Wang, On the chemical compatibility between Zr-4 substrate and well-bonded Cr_2AlC coating, J. Mater. Sci. Technol. 35 (2019) 1–5.

[14] W. Li, Z. Wang, J. Shuai, B. Xu, A. Wang, P. Ke, A high oxidation resistance Ti_2AlC coating on Zirlo substrates for loss-of-coolant accident conditions, Ceram. Int. 45 (2019) 13912–13922.

[15] C. Tang, M. Klimenkov, U. Jaentsch, H. Leiste, M. Rinke, S. Ulrich, M. Steinbrueck, H.J. Seifert, M. Stueber, Synthesis and characterization of Ti_2AlC coatings by magnetron sputtering from three elemental targets and ex-situ annealing, Surf. Coat. Technol. 309 (2017) 445–455.

[16] W.C. Bao, J.X. Xue, J.X. Liu, X.G. Wang, Y.F. Gu, F.F. Xu, G.J. Zhang, Coating SiC on Zircaloy-4 by magnetron sputtering at room temperature, J. Alloy. Compd. 730 (2018) 81–87.

[17] B. Maier, H. Yeom, G. Johnson, T. Dabney, J. Walters, P. Xu, J. Romero, H. Shah, K. Sridharan, Development of cold spray chromium coatings for improved accident tolerant zirconium-alloy cladding, J. Nucl. Mater. 519 (2019) 247–254.

[18] A. Michau, F. Maury, F. Schuster, F. Lomello, J.C. Brachet, E. Rouesne, M.Le Saux, R. Boichot, M. Pons, High-temperature oxidation resistance of chromium-based coatings deposited by DLI-MOCVD for enhanced protection of the inner surface of long tubes, Surf. Coat. Technol. 349 (2018) 1048–1057.

[19] H.-G. Kim, I.-H. Kim, Y.-I. Jung, D.-J. Park, J.-Y. Park, Y.-H. Koo, Adhesion property and high-temperature oxidation behavior of Cr-coated Zircaloy-4 cladding tube prepared by 3D laser coating, J. Nucl. Mater. 465 (2015) 531–539.

[20] J. Yang, M. Steinbrück, C. Tang, M. Große, J. Liu, J. Zhang, D. Yun, S. Wang, Review on chromium coated zirconium alloy accident tolerant fuel cladding, J. Alloy. Compd. 895 (2022) 162450.

[21] J.L. Lin, I. Dahan, Nanostructured chromium coatings with enhanced mechanical properties and corrosion resistance, Surf. Coat. Technol. 265 (2015) 154–159.

[22] F. Ferreira, R. Serra, J.C. Oliveira, A. Cavaleiro, Effect of peak target power on the properties of Cr thin films sputtered by HiPIMS in deep oscillation magnetron sputtering (DOMS) mode, Surf. Coat. Technol. 258 (2014) 249–256.

[23] Z. Wang, W. Li, Z. Wang, M. Li, A. Wang, P. Ke, Comparative study on protective Cr coatings on nuclear fuel cladding Zirlo substrates by AIP and HiPIMS techniques, Ceram. Int. 49 (2023) 22736–22744.

[24] H.B. Ma, J. Yan, Y.H. Zhao, T. Liu, Q.S. Ren, Y.H. Liao, J.D. Zuo, G. Liu, M.Y. Yao, Oxidation behavior of Cr-coated zirconium alloy cladding in high-temperature steam above 1200 °C, NPJ Mater. Degrad. 5 (2021) 7.

[25] J.-S. Jiang, D.-Q. Wang, M.-Y. Du, X.-F. Ma, C.-X. Wang, X.-J. He, Interdiffusion behavior between Cr and Zr and its effect on the microcracking behavior in the Cr-coated Zr-4 alloy, Nucl. Sci. Tech. 32 (2021) 134.

[26] J.-C. Brachet, E. Rouesne, J. Ribis, T. Guilbert, S. Urvoy, G. Nony, C. Toffolon–Masclet, M.Le Saux, N. Chaabane, H. Palancher, A. David, J. Bischoff, J. Augereau, E. Pouillier, High temperature steam oxidation of chromium-coated zirconium-based alloys: kinetics and process, Corros. Sci. 167 (2020) 108537.

[27] C. Tang, M. Steinbrueck, M. Stueber, M. Grosse, X. Yu, S. Ulrich, H.J. Seifert, Deposition, characterization and high-temperature steam oxidation behavior of single-phase Ti_2AlC-coated Zircaloy-4, Corros. Sci. 135 (2018) 87–98.

[28] X. Wang, H. Guan, Y. Liao, M. Zhu, C. Xu, X. Jin, B. Liao, W. Xue, Y. Zhang, G. Bai, R. Wang, Enhancement of high temperature steam oxidation resistance of Zr–1Nb alloy with ZrO_2/Cr bilayer coating, Corros. Sci 187 (2021) 109494.

[29] M. Syrtanov, E. Kashkarov, A. Abdulmenova, K. Gusev, D. Sidelev, High-temperature steam oxidation of accident-tolerant Cr/Mo-coated Zr alloy at 1200-1400 °C, Coatings 13 (2023) 191.

[30] C. Gautier, J. Machet, Effects of deposition parameters on the texture of chromium films deposited by vacuum arc evaporation, Thin Solid Films 289 (1996) 34–38.

[31] J.M. Zhang, K.W. Xu, M.R. Zhang, Theory of abnormal grain growth in thin films and analysis of energy anisotropy, Acta Phys. Sin. 52 (2003) 1207–1212.

[32] A. Anders, A review comparing cathodic arcs and high power impulse magnetron sputtering (HiPIMS), Surf. Coat. Technol. 257 (2014) 308–325.

[33] X. Zuo, P.L. Ke, R.D. Chen, X.W. Li, M. Oden, A.Y. Wang, Discharge state transition and cathode fall thickness evolution during chromium HiPIMS discharge, Phys. Plasmas 24 (2017) 083507.

[34] H. Yeom, B. Maier, G. Johnson, T. Dabney, M. Lenling, K. Sridharan, High temperature oxidation and microstructural evolution of cold spray chromium coatings on Zircaloy-4 in steam environments, J. Nucl. Mater. 526 (2019) 151737.

[35] V.F. Urbanic, T.R. Heidrick, High-temperature oxidation of zircaloy-2 and zircaloy-4 in steam, J. Nucl. Mater. 75 (1978) 251–261.

[36] J. Jiang, M. Du, X. Ma, On the microstructures and cracking modes of Cr-coated Zr-4 alloys oxidized and vacuum-annealed at 1000°C, J. Alloy. Compd. 908 (2022) 164610.

[37] Z.Y. Liu, W. Gao, M.S. Li, Cyclic oxidation of sputter-deposited nanocrystalline Fe-Cr-Ni-Al alloy coatings, Oxid. Met. 51 (1999) 403–419.